Draft version January 13, 2022
Typeset using LaTeX **twocolumn** style in AASTeX631

A Mirage or an Oasis? Water Vapor in the Atmosphere of the Warm Neptune TOI-674 b

Jonathan Brande [1], Ian J. M. Crossfield,[1] Laura Kreidberg [2], Antonija Oklopčić,[3] Alex S. Polanski [1], Travis Barman,[4] Björn Benneke,[5] Jessie L. Christiansen [6], Diana Dragomir,[7] Daniel Foreman-Mackey [8], Jonathan J. Fortney [9], Thomas P. Greene [10], Andrew W. Howard [11], Heather A. Knutson [12], Joshua D. Lothringer [13], Thomas Mikal-Evans,[2] and Caroline V. Morley [14]

[1] *Department of Physics and Astronomy, University of Kansas, 1082 Malott, 1251 Wescoe Hall Dr., Lawrence, KS 66045, USA*
[2] *Max Planck Institute for Astronomy, Königstuhl 17, 69117 Heidelberg, Germany*
[3] *Anton Pannekoek Institute of Astronomy, University of Amsterdam, Science Park 904, 1098 XH Amsterdam, Netherlands*
[4] *Lunar and Planetary Laboratory, University of Arizona, Tucson, AZ 85721 USA*
[5] *Departement de Physique, and Institute for Research on Exoplanets, Universite de Montreal, Montreal, Canada*
[6] *Caltech/IPAC-NASA Exoplanet Science Institute, Pasadena, CA 91125, USA*
[7] *Department of Physics and Astronomy, University of New Mexico, Albuquerque, NM, USA*
[8] *Center for Computational Astrophysics, Flatiron Institute, New York, NY 10010, USA*
[9] *Department of Astronomy and Astrophysics, University of California, Santa Cruz, CA 95064, USA*
[10] *NASA Ames Research Center Space Science and Astrobiology Division M.S. 245-6 Moffett Field, CA 94035, USA*
[11] *Cahill Center for Astronomy & Astrophysics, California Institute of Technology, Pasadena, CA 91125, USA*
[12] *Division of Geological and Planetary Sciences, California Institute of Technology, Pasadena, CA 91125, USA*
[13] *Physics Department, Utah Valley University, 800 West University Parkway, Orem, UT 85058-5999, USA*
[14] *Department of Astronomy, University of Texas at Austin, Austin, TX, USA*

ABSTRACT

We report observations of the recently discovered super-Neptune TOI-674 b (5.25 $R_\oplus$, 23.6 $M_\oplus$) with the Hubble Space Telescope's Wide Field Camera 3 instrument. TOI-674 b is deep into the Neptune desert, an observed paucity of Neptune-size exoplanets at short orbital periods. Planets in the desert are thought to have complex evolutionary histories due to photoevaporative mass loss or orbital migration, making identifying the constituents of their atmospheres critical to understanding their origins. We obtained near-infrared transmission spectroscopy of the planet's atmosphere with the G141 grism, which we detrended and fit. After extracting the transmission spectrum from the data, we used the petitRADTRANS atmospheric spectral synthesis code to perform retrievals on the planet's atmosphere to identify which absorbers are present. These results show evidence for increased absorption at 1.4 μm due to water vapor at 2.1σ (Bayes factor = 3.2). With these results, TOI-674 b joins the exclusive club of exoplanets with featured transmission spectra. TOI-674 b is a strong candidate for further study to refine the water abundance, which is poorly constrained by our data. We also incorporated new TESS short-cadence optical photometry, as well as Spitzer/IRAC data, and re-fit the transit parameters for the planet. We find the planet to have the following transit parameters: $R_p/R_* = 0.1135 \pm 0.0006$, $T_0 = 2458544.523792 \pm 0.000452$ BJD, and $P = 1.977198 \pm 0.00007$ d. These measurements refine the planet radius estimate and improve the orbital ephemerides for future transit spectroscopy observations of this highly intriguing warm Neptune.

Keywords: Exoplanet atmospheres (487) — Exoplanet atmospheric composition (2021) — Transmission spectroscopy (2133) — M stars (985) — Near infrared astronomy (1093) — Hubble Space Telescope (761)

1. INTRODUCTION

The last two and a half decades of exoplanet science have revealed a wealth of information on planetary

Corresponding author: Jonathan Brande
jbrande@ku.edu

system architectures. The first discovered exoplanet around a Sun-like star, 51 Pegasi b (Mayor & Queloz 1995) is a Hot Jupiter, one of a class of planets that challenged our ideas on the formation and evolution of planetary systems. As the field has progressed, these astonishing outliers have proven to be representative of larger planetary populations in systems often unlike our own.

In addition to these populations, several gaps in the distribution of short-period exoplanets have also been noted, namely the photoevaporation valley (Fulton et al. 2017) and the Neptune desert (Mazeh et al. 2016). For the photoevaporation valley, atmospheric mass loss due to host star irradiation is the main theory for the observed lack of 1.5–2 $R_\oplus$ planets at these short orbital periods (Owen & Wu 2017). Other explanations due to formation mechanisms and core-powered mass loss (Ginzburg et al. 2018) have also been put forth, as well as a primordial radius gap due to late gas accretion in gas-poor nebulae (Lee & Connors 2021). The Neptune desert is a similar lack of planets at even shorter orbital periods ($P \leq 3$ d) but for approximately Neptune-to-Jupiter mass planets. The lower-mass section of the gap may be appropriately explained by irradiative atmospheric stripping, but the dearth of Jupiter-mass planets in this narrow period range may be better explained by planetary migration and in-situ formation (Owen & Lai 2018; Bailey & Batygin 2018).

The Neptune desert is especially relevant, given the uncertainties in our own solar system about the formation of Uranus and Neptune, either through core accretion (Frelikh & Murray-Clay 2017) or disk instability (Boss 2003). We presume migration processes were important in their early histories as they would have been for Jupiter and Saturn, and by proxy also the observed exoplanetary populations. However, compared to the current observed sample of exoplanets, we find very few exoplanets with similar masses and orbital separations as Uranus and Neptune have in our own solar system, although this is certainly incomplete due to a lack of observational sensitivity for low-mass, widely separated planets. Most known planets in this mass range (10–40 $M_\oplus$) are relatively evenly distributed at intermediate separations, but populations at short orbital separations and wide orbital separations (including Uranus and Neptune) seem similarly sparse.

As can be seen in Fig. 1, fewer total planets with measured masses are known to orbit M-dwarfs than other stellar types, making it difficult to say with certainty whether the Neptune desert exists around the coolest stars. As the upper boundary of the Neptune desert is characterized by planets with masses $\lesssim M_{Jup}$, the upper bound for the M-dwarf Neptune desert is unclear given the general lack of massive planets around M-dwarfs. However, the lower boundary of the desert appears to hold for the M-dwarf planet population.

It is especially tempting to want to characterize the few large planets known to exist in the desert. Several high profile planet discoveries have been made in the Neptune desert (Bakos et al. 2010; Hartman et al. 2011; Jenkins et al. 2020; West et al. 2019; Barragán et al. 2018; Eigmüller et al. 2017; Crossfield et al. 2016; Bakos et al. 2015; Bonomo et al. 2014; Borucki et al. 2010), and these "Nomads" (so-called due to their presence in the desert, as well as their possible migratory histories) may be exceptional in several ways. Young Nomads may be undergoing atmospheric mass loss, or may be in the process of migrating into the desert. Older Nomads may have already lost parts of their atmospheres, or finished their migrations. However, as this is only a relatively recently identified population, only a few Nomads have been characterized by atmospheric transmission spectroscopy (Fraine et al. 2014; Wakeford et al. 2017). Here we present Hubble Space Telescope (*HST*) Wide Field Camera 3 (WFC3) spectroscopic observations of the recently discovered super-Neptune Nomad TOI-674 b.

1.1. *TOI-674 b*

The TESS observatory recently discovered TOI-674 b, a super-Neptune (5.25 $R_\oplus$, 23.6 $M_\oplus$) orbiting a nearby M2 dwarf (TIC 158588995, V=14.2 mag, J=10.4 mag, RA $10^h58^m20.98^s$ DEC -36°51′29.13″ (J2000), 46.16 pc, 0.420 $R_\odot$, 0.420 $M_\odot$; Stassun et al. 2018) with a period of 1.977143 days (Murgas et al. 2021). With these parameters, TOI-674 b is deep into the Neptune desert (see Fig. 1).

TOI-674 b also provides a good target for atmospheric transmission spectroscopy, which attracted our attention during the first year of the TESS mission. Given the small size of the host star and relatively large radius of the planet, TOI-674 b has a high transmission spectroscopy metric of 222 (see Kempton et al. (2018) for a definition of this quantity). Compared to other similar planets in the desert (see e.g. Fig. 10 in Murgas et al. 2021), these factors make it one of the best planets of its class for transmission spectroscopy.

2. DATA, DATA REDUCTION, AND ANALYSIS

2.1. *Observations*

We observed three transits of TOI-674 b on 10, 12, and 26 July 2020 with the *Hubble Space Telescope's* (*HST*) Wide Field Camera 3 instrument, as part of the large *HST* General Observer Program 15333 (Co-PIs: Crossfield and Kreidberg). Each transit visit consisted of four

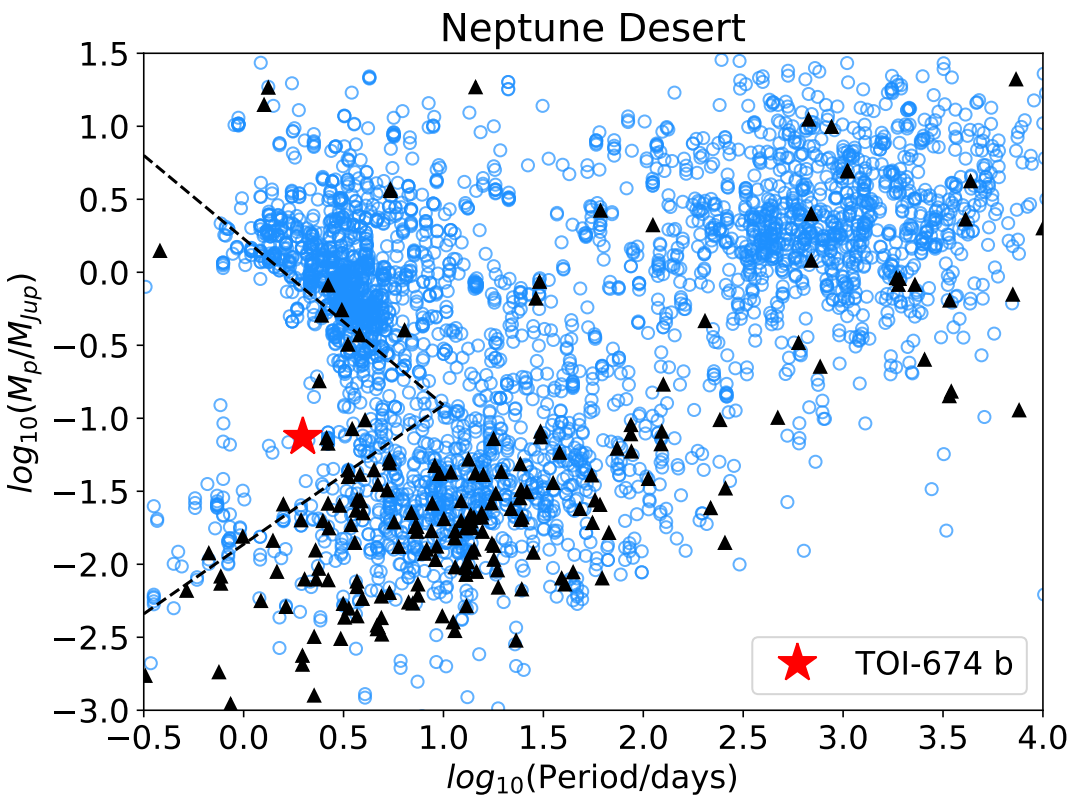

Figure 1. Planet mass vs period for all planets with known masses and periods. The dashed black lines show the boundaries of the Neptune desert from (Mazeh et al. 2016), the black triangles show M-star planets, the blue circles show all stellar hosts, and the red star shows TOI-674 b.

orbits, and each orbit started with one direct image in the F130N filter, and then continued with spectroscopic imaging with the G141 grism. The spectroscopic frames were spatially scanned (McCullough & MacKenty 2012; Deming et al. 2013). As TOI-674 b was discovered by the Transiting Exoplanet Survey Satellite (*TESS*) (Ricker et al. 2015), we also have access to planet transit data in the *TESS* bandpass, including new observations in *TESS* year 3 that were not incorporated in the discovery paper. Finally, we also observed a single transit of TOI-674 b with the *Spitzer* Space Telescope (also incorporated into (Murgas et al. 2021). We incorporate both the *TESS* and *Spitzer* transit depths into our eventual atmospheric retrievals (see Sec. 3).

2.2. *Data Reduction and Analysis*

We used the `Iraclis` pipeline (Tsiaras et al. 2016a,b, 2018) to reduce the raw spatially scanned *HST* data and extract spectral lightcurves. `Iraclis` performs a standard set of *HST* WFC3 image reduction steps and then extracts the spectrum from the reduced images. `Iraclis` ingests *HST* flat-fielded direct images of the target star to locate the target on the detector, and then extracts the spatially scanned spectrum from the raw spectral data files. After conducting the reduction and extraction, `Iraclis` returns the reduced images and extracted spectra, along with some diagnostic information. Input parameter files allow a user to modify various aspects of the reduction, extraction, and fitting process. We optimized the extraction aperture to minimize the scatter in the spectrophotometric lightcurves, and used an aperture that extended 10 pixels above and below the observed spectrum. We extracted 18 spectral bins ranging from 1.1108 μm to 1.6042 μm. The extracted lightcurves were then used as inputs for our transit model and systematics fitting process.

2.2.1. *Transit and Systematics Models*

HST/WFC3 lightcurves offer precise transit measurements but are known to be subject to significant systematic effects. In order to detrend the transit lightcurves we modified the `model-ramp` method from Kreidberg et al. (2014) to fit our data. Our modification of the `model-ramp` method fits the systematics and the transit parameters simultaneously as follows:

$$M_{\lambda v}(t) = F_{\lambda v}[M_{0,\lambda}(t)(1 + V_{\lambda v}\mathbf{t_v})(1 - R_{\lambda v}e^{-\mathbf{t_v}/\tau_\lambda}) + (S_{\lambda vo}\cos\frac{\pi \mathbf{t_b}}{\tau_c})] \quad (1)$$

$M_{\lambda v}(t)$ is the full model to the observed data, $F_{\lambda v}$ is the out-of-transit mean flux, $M_{0,\lambda}(t)$ is the bare normalized transit lightcurve, $V_{\lambda v}$ is a visit-long slope, $R_{\lambda vo}$ is the amplitude of the ramp systematic, τ_λ is the ramp systematic timescale, $\mathbf{t_v}$ is a vector of the times elapsed since the first exposure in the current visit, $S_{\lambda vo}$ the amplitude of the scan-direction sinusoid, $\mathbf{t_b}$ a vector of the times elapsed since the first exposure in the current orbit, and τ_c the average duration between the start of each exposure. λ, v, o are subscripts denoting spectral bin central wavelength, *HST* visit, and orbit number.

Following previous analyses, we discard the initial orbit in each visit due to the strong effect of the ramp systematic in that orbit, and we also found that the initial spectral exposure in each orbit was also strongly affected by the ramp systematic and discarded it as well. Using the `exoplanet` toolkit (Foreman-Mackey et al. 2021), we fit the white-light transit lightcurves for each transit, fitting the exponential orbit-level ramp and visit-long slope systematics models as described in Kreidberg et al. (2014), and correcting for the up/down scan directions with a sinusoidal model. Spatially-scanned WFC3 data has a significant flux offset as the target star is scanned up or down the detector. Previous work has fit these scan directions independently and then combined both scan-direction lightcurves to find the true transit model. The sinusoidal approach allows both scan directions to be fit in the same operation for better modeling efficiency. The transit lightcurve and systematics parameters are normalized such that the out of transit flux is 1, and then the entire model is multiplied by the mean out of transit flux observed in the *HST* data.

Our *HST* transit model incorporated the published star and planet parameters from Murgas et al. (2021), except where those parameters were refined by our new fit to the *TESS* data incorporating Sector 36. The stellar and planetary parameter priors are shown in Table. 1. Limb darkening coefficients for the broadband transit and spectral bins were pre-calculated using the Limb Darkening Calculator in the Exoplanet Characterization Toolkit (ExoCTK) (Bourque et al. 2021), using the published stellar parameters from Murgas et al. (2021), and the Kurucz ATLAS9 stellar models. All parameter estimation was conducted with the `exoplanet` toolkit (Foreman-Mackey et al. 2021), built on top of PyMC3 (Salvatier et al. 2016) for posterior sampling.

After modeling the WFC3 broadband transit lightcurves, we used our derived transit and systematics parameters to inform our spectral lightcurve models and fit each of these individually, yielding the full transit spectrum. We also checked our transits for correlated noise by binning the data between 1 and 20 points and calculating the rms for each bin size. Fig. 3 shows the RMS trend deviation for each spectral lightcurve bin in each visit. The expected trend due to uncorrelated noise is $\sqrt{N_{phot}}$, and our measured RMS error generally follows the uncorrelated noise trend, even though the bin sizes are relatively small. After fitting each visit, we averaged the spectra together in order to obtain the full transmission spectrum of the planet. The measured transit depths and their uncertainties are shown in Table 2. Fig. 2 shows the final averaged spectrum from TOI-674 b, as well as the individual spectra for each *HST* visit. Visit 3 notably has higher transit depth between 1.2 μm and 1.45 μm, but does not significantly bias the final average spectrum.

Table 1. LC and Systematics Fitting Priors

Parameter	Prior
T_0 (BJD)	$\mathcal{N}(2458641.405, 0.0104)$
r_p/r_*	Lognormal(ln(0.11355), ln(0.001))
$^*P$ (d)	1.977198
$^*e$	0.0
$^*\omega$	0.0
$F_{\lambda v}$	Lognormal(μ_{oot}, ln(σ_F))
$V_{\lambda v}$	$\mathcal{N}(0, 0.001)$
$R_{\lambda vo}$	$\mathcal{N}(0.001, 0.0001)$
τ_λ	Lognormal($\frac{\tau_0}{2}$, 1.0)
$S_{\lambda vo}$	$\mathcal{U}(0, 1)$

NOTE—Rows marked with * denote fixed values in the transit fit. μ_{oot} is the mean out-of-transit flux, σ_F is $\frac{max(F_{oot})-min(F_{oot})}{4}$, and τ_0 is the duration of the first visit.

2.2.2. *Independent Analysis*

In addition to our method, we also used Iraclis's transmission spectroscopy modeling capabilities to conduct an independent analysis of the data. Iraclis also fits individual *HST* visits, and uses the `divide-white` method as described in Kreidberg et al. (2014). Again, we took the unweighted average of the individual visits to obtain the transmission spectrum for our entire dataset. We found that the Iraclis results were consistent with our own analysis, which validates our modeling approach.

2.2.3. *Spitzer and TESS Data Points*

TOI-674 b was originally observed in *TESS* Sectors 9 and 10. The discovery paper included data from these

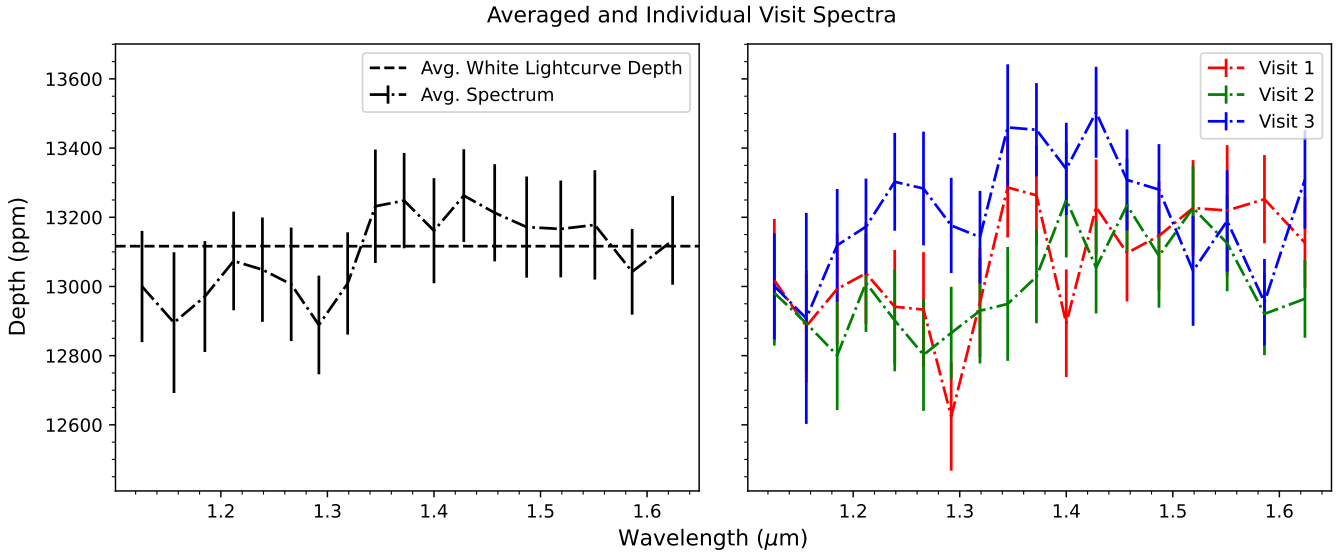

Figure 2. Unweighted average spectrum for TOI-674 b based on all three *HST* visits, and the spectra in each individual visit.

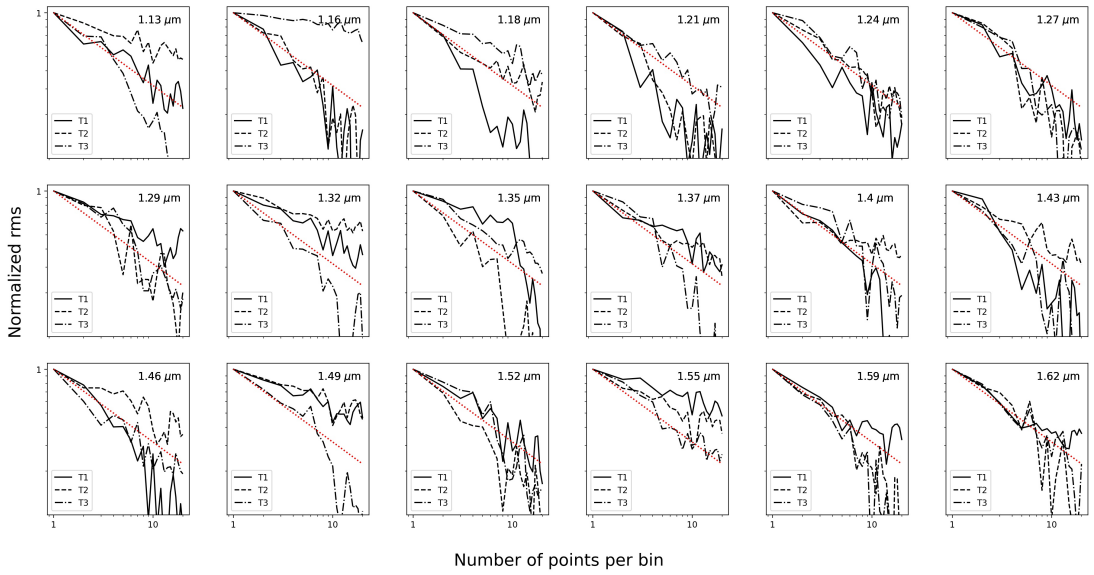

Figure 3. RMS deviation plot, as a function of bin size for each observed transit of TOI-674 b. The dotted red line shows the expected $\sqrt{N}$ trend for uncorrelated noise, and the black lines show the normalized RMS trend.

two sectors, but TOI-674 b was also observed in *TESS* Sector 36, from 2021 March 7, to 2021 April 1. We re-fit the *TESS* data including the new sector of data in order to refine the observed and derived transit parameters, including a search for transit timing variations (TTVs) that could show evidence of undiscovered companions to TOI-674 b. Including the Sector 36 data, we found $T_0 = 2458544.523792 \pm 0.000452$ BJD and $P = 1.977198 \pm 0.00007$ d. The results of the TTV analysis are shown in Figure 4. The O-C diagram shows that the transit times are consistent with a linear ephemeris, in agreement with the analysis performed in the original discovery paper. Even without a detection of a new planet in the system, the refined transit parameters and ephemerides will be useful for further studies of this planet.

Also, as reported in the discovery paper, a single transit of TOI-674 b was observed by the *Spitzer* Space Telescope on 2019 September 29 as part of a program dedicated to IRAC follow-up of *TESS* planet candidates (GO-14084, PI: Crossfield). TOI-674 b was observed at 4.5 μm using *Spitzer*'s IRAC instrument (Fazio et al. 2004). Using the updated parameters from the full *TESS* transit fit as priors, we reanalyzed the archival *Spitzer* data. Both the *TESS* and *Spitzer* transit fit results are shown in Table 3. We incorporate the *TESS* and *Spitzer* transit depths into our observed WFC3

Table 2. Transit depths, transit depth errors, and limb-darkening coefficients for each spectral bin in the *TESS*, *HST*, and *Spitzer* data.

Wavelength (μm)	Depth (ppm)	Error (ppm)	u_1 (fixed)	u_2 (fixed)
0.600 – 1.000	12900	169	0.098	0.248
1.111 – 1.142	13000	159	0.117	0.286
1.142 – 1.171	12895	204	0.114	0.278
1.171 – 1.199	12970	160	0.111	0.275
1.199 – 1.226	13074	142	0.109	0.268
1.226 – 1.252	13047	150	0.109	0.261
1.252 – 1.279	13004	165	0.107	0.259
1.279 – 1.306	12887	143	0.104	0.256
1.306 – 1.332	13008	148	0.102	0.251
1.332 – 1.359	13233	163	0.100	0.247
1.359 – 1.386	13248	135	0.099	0.243
1.386 – 1.414	13161	152	0.096	0.240
1.414 – 1.442	13263	136	0.094	0.238
1.442 – 1.472	13214	140	0.092	0.237
1.472 – 1.503	13172	146	0.088	0.234
1.503 – 1.534	13164	141	0.085	0.230
1.534 – 1.568	13178	157	0.081	0.227
1.568 – 1.604	13042	125	0.074	0.223
1.604 – 1.643	13131	130	0.070	0.210
3.917 – 5.056	13317	1800	0.041	0.170

Table 3. *TESS* and *Spitzer* Transit Fits

Parameter	Value	Error
TESS Observed Parameters		
T_0 (BJD)	2458544.523792	0.000452
P (d)	1.977198	0.00007
R_p/R_*	0.1135	0.0006
b	0.682	0.006
TESS Derived Parameters		
a (AU)	0.0231	0.0000003
a/R_*	11.821	0.0002
i (deg)	86.69	0.03
R_p ($R_\oplus$)	5.20	0.030
Spitzer Observed Parameters		
T_0 (BJD)	2458756.0796	0.00012
R_p/R_*	0.1154	0.0009
b	0.651	0.063
Spitzer Derived Parameters		
a (AU)	0.0243	0.0012
a/R_*	12.44	0.46
i (deg)	87.00	0.27
R_p ($R_\oplus$)	5.29	0.17
Spitzer Quad. Limb Darkening		
u_1	0.0412	
u_2	0.170	

NOTE—Parameters without stated ranges were fixed in the transit fit.

spectrum for the purposes of our later atmospheric retrievals.

3. ATMOSPHERIC RETRIEVALS

3.1. *petitRADTRANS*

We used `petitRADTRANS` (pRT), an open-source atmospheric spectral synthesis package (Mollière et al. 2019, 2020) to conduct our atmospheric retrievals. `petitRADTRANS` can be combined with several sampling packages to conduct atmospheric retrievals, and we used the suggested configuration by combining it with `PyMultiNest` (Buchner et al. 2014), a Python-based implementation of the MultiNest nested sampling code (Feroz et al. 2009).

In order to determine what molecules might be present in TOI-674 b's atmosphere, we conducted free chemistry retrievals for the abundances of specific atmospheric species, namely H_2O, CH_4, CO, CO_2, and NH_3 following (Benneke & Seager 2013), as these are some of the dominant opacity sources in the NIR. We also fit for the presence or absence of clouds, here represented as a uniform opaque gray cloud at a specific atmospheric pressure. The full model incorporating all of the absorbers is compared to models removing one absorber at a time, and if the model without that absorber is less favored than the full model, we can say that the absorber is likely present. Prior distributions for our retrievals are shown in Table 4.

We fixed the stellar radius, set uniform priors on the planet's radius, and temperature, and log-uniform priors on the planet's gravity, mass fraction of each absorber, and the cloudtop pressure. The retrievals were conducted using isothermal atmospheric models to create the planet spectra. Without proper bounds on the planetary temperature, the atmospheric retrievals may find non-physical temperatures for this planet. In order to avoid this, we bound the temperature prior with some reasonable assumptions. The equilibrium temper-

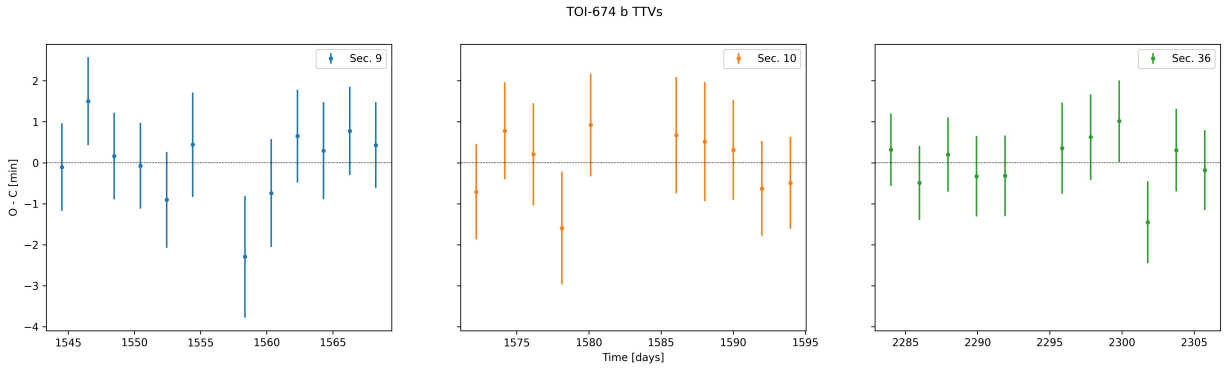

Figure 4. Observed minus calculated transit times for TOI-674 b across all sectors of *TESS* data. The transit times do not significantly deviate from a linear ephemeris.

Table 4. Retrieval Priors

Parameter	Prior
log(g) log(cm/s^2)	$\mathcal{U}(2.85, 3.0)$
R_p (R_{Earth})	$\mathcal{U}(5.0, 5.5)$
T (K)	$\mathcal{U}(600, 900)$
log(P_{cloud}) log(bar)	$\mathcal{U}(-6.0, 2.0)$
H_2O log(mass frac)	$\mathcal{U}(-6.0, 0.0)$
CH_4 log(mass frac)	$\mathcal{U}(-6.0, 0.0)$
CO log(mass frac)	$\mathcal{U}(-6.0, 0.0)$
CO_2 log(mass frac)	$\mathcal{U}(-6.0, 0.0)$
NH_3 log(mass frac)	$\mathcal{U}(-6.0, 0.0)$

ature of a planet can be estimated either with or without incorporating heat redistribution:

$$T_{\rm eq} = \sqrt{\frac{R_*}{a}}(1-A)^{1/4} T_{\rm eff}$$

Or:

$$T_{\rm eq} = \sqrt{\frac{R_*}{a}}[f(1-A)]^{1/4} T_{\rm eff}$$

Where f is a measure of heat redistribution in the range $[\frac{1}{4}, \frac{2}{3}]$ (Seager 2010). Without incorporating heat redistribution, and assuming a planetary albedo of 0.3, Murgas et al. (2021) estimated the equilibrium temperature of the planet to be ~ 635 K. Assuming an albedo range of $A \in [0, 0.5]$, including the extreme bounds of heat redistribution, and for the stellar $T_{\rm eff} = 3514$ K, we calculate that the planet $T_{\rm eq} \in [600, 900]$ K.

Each retrieval has an associated Bayesian evidence value Z, and the ratio of two evidences gives the Bayes factor K:

$$K = \frac{Z_0}{Z}$$

where Z_0 is the model evidence for the full model, and Z is the model evidence for a particular retrieval missing an absorber. Following Trotta (2008), Bayes factors can be converted to p-values, and then standard deviations, by the formulas:

$$K = -\frac{1}{e(p \ln p)}$$

where K is the Bayes factor and p the p-value, and:

$$p = 1 - \mathrm{erf}\left(\frac{n_\sigma}{\sqrt{2}}\right)$$

where n_σ is the sigma significance and erf is the error function. Trotta (2008) and Benneke & Seager (2013) present ranges of Bayes factors that correspond to p-values and sigma significances, with $2.9 \leq K < 12$ ($2.1\sigma \leq n_\sigma < 2.7\sigma$) a "weak detection", $12 \leq K < 150$ ($2.7\sigma \leq n_\sigma < 3.6\sigma$) a "moderate detection", and $K \geq 150$ ($n_\sigma \geq 3.6\sigma$) a "strong detection". The Bayes factor analysis results are shown in Table 5. We find that the presence of H_2O is favored with a Bayes factor of 3.2, corresponding to a 2.1σ detection, whereas the evidence for the other absorbers, including the cloud, is insignificant. We also present the best-fit values for the full model in Table 6.

3.1.1. *Utility of Equilibrium Chemistry Models*

Previous theoretical (Moses et al. 2013) and observational work on Neptune-sized exoplanets has revealed a diversity of potential atmospheric compositions, even for the handful for which there are measured transmission spectra (e.g. HAT-P-11 b (Fraine et al. 2014), HAT-P-26 b (Wakeford et al. 2017), GJ 436 b (Knutson et al. 2014), and GJ 3470 b (Benneke et al. 2019)). Interestingly, these planets have been observed to have very diverse metallicities, ranging from near solar (Benneke et al. 2019) to high metallicity (Morley et al. 2017), suggesting varied planet formation processes. Ordinarily it would be desirable to use equilibrium chemistry models

to fit for the metallicity of the planet and then determine the abundances of atmospheric species, but these predictions may not be consistent with observations due to nonequilibrium processes (see e.g. Fortney et al. (2020) for a detailed treatment of the varied observable tracers) or unknown formation history (Benneke et al. 2019). Given these theoretical and observational uncertainties, we do not attempt to constrain the atmospheric metallicity of TOI-674 b.

4. DISCUSSION

4.1. *Atmospheric Compositions*

Although the retrieval analysis is useful for identifying the presence of particular absorbers, our data are not precise enough to allow us to precisely measure the abundances of any absorbers present. In this case, a range of H_2O abundances is likely to be consistent with the data, as seen in Table 6. Each absorber has at least an order of magnitude uncertainty in the mass fraction, and some (like CO_2 and CO), have error bars of two orders of magnitude. Assuming a mean molecular weight $\mu = 3.0$ amu (corresponding to $\sim 30\times$ Solar metallicity), we estimate a scale height H $\sim$ 260 km, approximately equal to 100 ppm transit depth per scale height. The amplitude of the 1.4μm water feature here is $\sim$ 2 scale heights, somewhat higher than expected from the trend in Crossfield & Kreidberg (2017) given the range of possible equilibrium temperatures for TOI-674 b. Further work will explore this trend in more detail including the updated sample of Neptune-sized exoplanets with measured transmission spectra. The prominence of these features is likely to be dependent on both cloudtop pressure and atmospheric metallicity. For example, both a solar metallicity atmosphere with a 0.01 bar cloud and a 300$\times$ solar metallicity clear atmosphere are consistent with our observed *HST* data. A significant diversity of atmospheric metallicities are predicted from formation modeling, from very high metallicities (Fortney et al. 2013), to very low (Bitsch et al. 2021), depending on where and how the planet formed in its disk, and whether it migrated relative to the the frost lines. Higher resolution, higher photometric precision data from a larger telescope will be critical to constraining TOI-674 b's atmospheric metallicity to inform planetary formation models. The recently launched James Webb Space Telescope will be able to acquire much better quality data across a larger NIR bandpass than can currently be collected by *HST*, allowing access to distinct H_2O, CH_4, and CO_2 features across the NIRISS, NIRSpec, and MIRI bandpasses (see Fig. 7, and Greene et al. (2016) for an observability study). CO_2 in particular is a tempting molecule to detect, as it is a better tracer of atmospheric metallicity than H_2O (Moses et al. 2013).

4.2. *Possible Helium Escape Observations*

In addition to future space-based near- and mid-infrared transmission spectroscopy, there is also room to further characterize TOI-674 b and its relatively unique place as an M-dwarf planet in the Neptune desert. As a low-mass Nomad, TOI-674 b is likely to be undergoing or have undergone potentially significant atmospheric escape due to stellar irradiation. One such tracer for this evolutionary process is the metastable helium line at 10830 Å (Oklopčić & Hirata 2018). The WFC3 G102 grism can measure the potential metastable helium transit of TOI-674 b from space (WASP-107 b; Spake et al. 2018), and metastable helium exospheres have also been observed with ground-based high-resolution spectrographs (HAT-P-11 b; Allart et al. 2018). With this in mind, we simulated the expected helium absorption signature.

4.2.1. *Atmospheric Simulations*

To estimate the expected absorption signature in the 10830 Å line triplet of neutral helium, we simulate the atmosphere of TOI-674 b using a spherically symmetric atmospheric escape model (Oklopčić & Hirata 2018). The density and velocity profiles of the escaping atmosphere are based on the isothermal Parker wind (Parker 1958; Lamers et al. 1999) and the model atmosphere is composed entirely of atomic hydrogen and helium, with a 9:1 number ratio. The main free parameters are the temperature of the upper atmosphere and the total mass loss rate, but without information on the high-energy luminosity of the host star, it is difficult to constrain their values. If we assume that the stellar spectrum is similar to that of GJ 176, an M2.5-type star observed as part of the MUSCLES survey (France et al. 2016), the energy-limited mass-loss rate would be on the order of 10^{10} g s^{-1}.

We run a grid of models spanning a range of thermosphere temperatures between 4,000 K and 9,000 K, and mass-loss rates between 10^9 g s^{-1} and $10^{11.5}$ g s^{-1}. We perform radiative transfer calculations along the planet's terminator, using the MUSCLES spectrum of GJ 176 as input, in order to calculate the abundance of helium atoms in the excited 2^3S state and the resulting opacity at 10830 Å. Finally, we compute the transmission spectrum for the planet at mid-transit. The predicted excess absorption depths vary substantially depending on the

Table 5. Bayesian Evidences for Various Retrieval Scenarios

Retrieval Model	$\log_{10}(Z)$	$\Delta \log_{10}(Z)$	Bayes Factor for molecule present
Full Model			
H2O, CH4, CO, CO2, NH3, Cloudy	-4.2	+0.0	+1.0
No H_2O	**-4.7**	**+0.5**	**+3.2**
No Cloud	-4.5	+0.3	+2.0
No CO_2	-4.2	+0.0	+1.0
No NH_3	-4.1	-0.1	+0.8
No CO	-4.1	-0.1	+0.8
No CH_4	-4.0	-0.2	+0.6

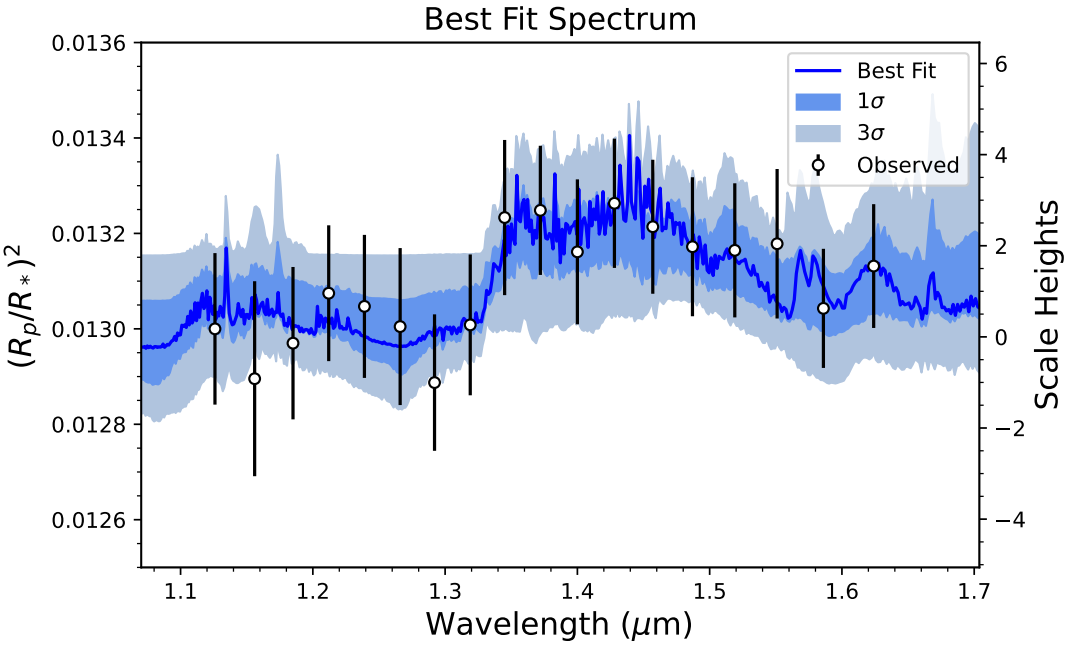

Figure 5. 3- and 1-sigma intervals for the full model. The solid blue line is the best fit model from the full retrieval.

assumed model parameters (as shown in Fig. 8), but in many cases the level of absorption is quite high, on the order of several percent at the line center, making this planet potentially interesting for helium 10830 Å observations.

5. CONCLUSIONS

TOI-674 b joins the club of planets with measured transmission spectra, and the even more exclusive club of planets for which those spectra are not flat. Only three other Neptune-size planets (masses between 10 and 40 Earth masses) have notable features in their atmospheres (WASP-107 b: Kreidberg et al. (2018); Spake et al. (2018), HAT-P-11 b: Fraine et al. (2014), and HAT-P-26 b: Stevenson et al. (2016)). With water present in its atmosphere, TOI-674 b is a good candidate for further study to determine the other components of its atmosphere, as well as potential tracers of atmospheric mass loss. Future work should concentrate on these efforts, especially as *TESS* continues to discover these types of exoplanets around nearby stars. Only by characterizing a large sample of Neptune-like exoplanets will we be able to more fully understand the formation and migratory processes that lead to the observed diverse population of exo-Neptune orbital architectures.

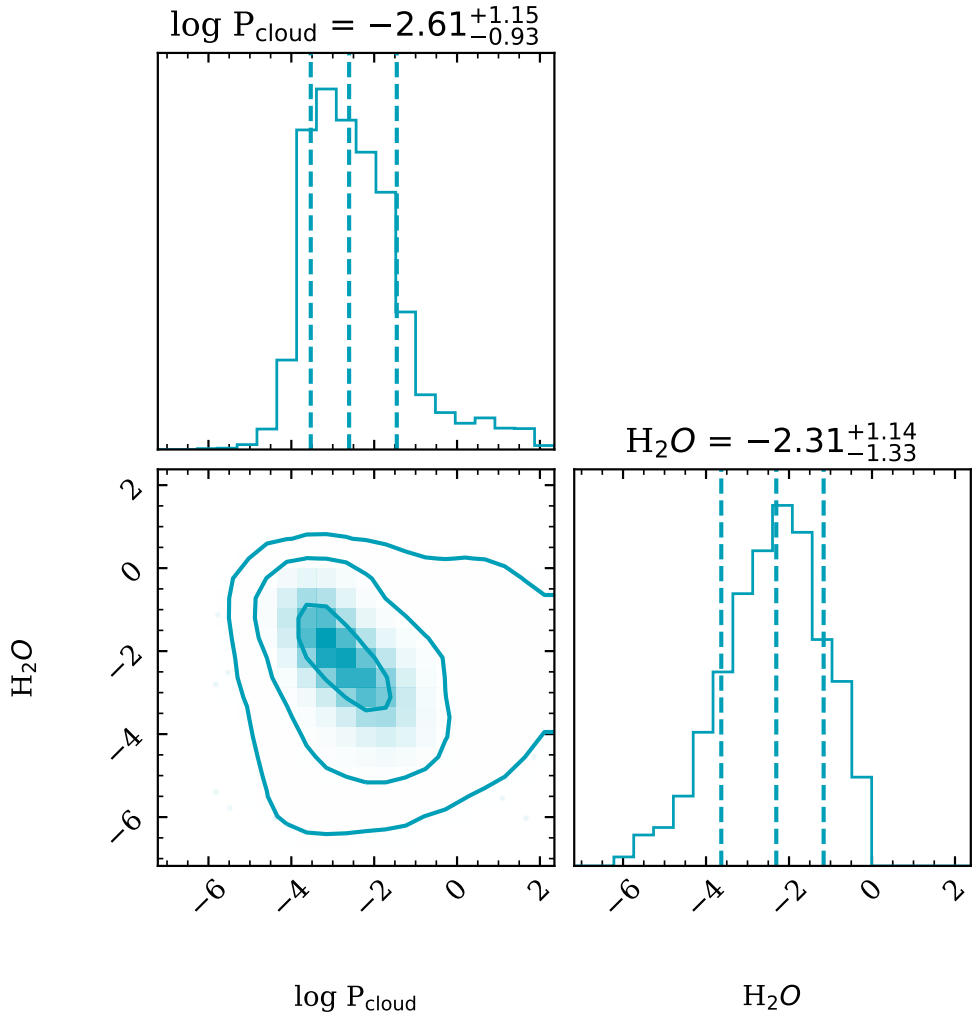

Figure 6. 2-D posteriors for the water abundance and cloudtop pressure. Cloudtop pressure is given in $\log_{10}$(bar), and water abundance is given in $\log_{10}$(mass mixing ratio).

We thank Paul Mollière and Evert Nasedkin for their extremely helpful assistance with petitRADTRANS. This research made use of the open source Python package ExoCTK, the Exoplanet Characterization Toolkit (Bourque et al. 2021).

APPENDIX

Facilities: HST, TESS, Spitzer, MAST, ExoFOP, Exoplanet Archive

Software: astropy (Astropy Collaboration et al. 2013, 2018), ExoCTK (Bourque et al. 2021), exoplanet (Foreman-Mackey et al. 2021), petitRADTRANS (Mollière et al. 2019, 2020), Iraclis (Tsiaras et al. 2016a,b, 2018)

Table 6. Full Atmospheric Model Results

Parameter	Fit Value
log(g) (cm/s^2)	2.9 ± 0.04
$R_{pl}(R_{Earth})$	5.22 ± 0.08
T (K)	611 ± 86
H2O	-1.98 ± 1.2
CH4	-4.73 ± 1.3
CO	-5.16 ± 1.9
CO2	-0.37 ± 2.0
NH3	-3.84 ± 1.1
log(P$_{cloud}$) (bar)	-1.40 ± 1.0

Note—pRT abundances are given as $\log_1 0$(mass mixing ratio). These can be converted to volume mixing ratios by $n_i = X_i \frac{\mu}{\mu_i}$, where n_i is the VMR, X_i the mass fraction of a species, μ_i the molecular weight of the species, and μ the mean molecular weight of the atmosphere.

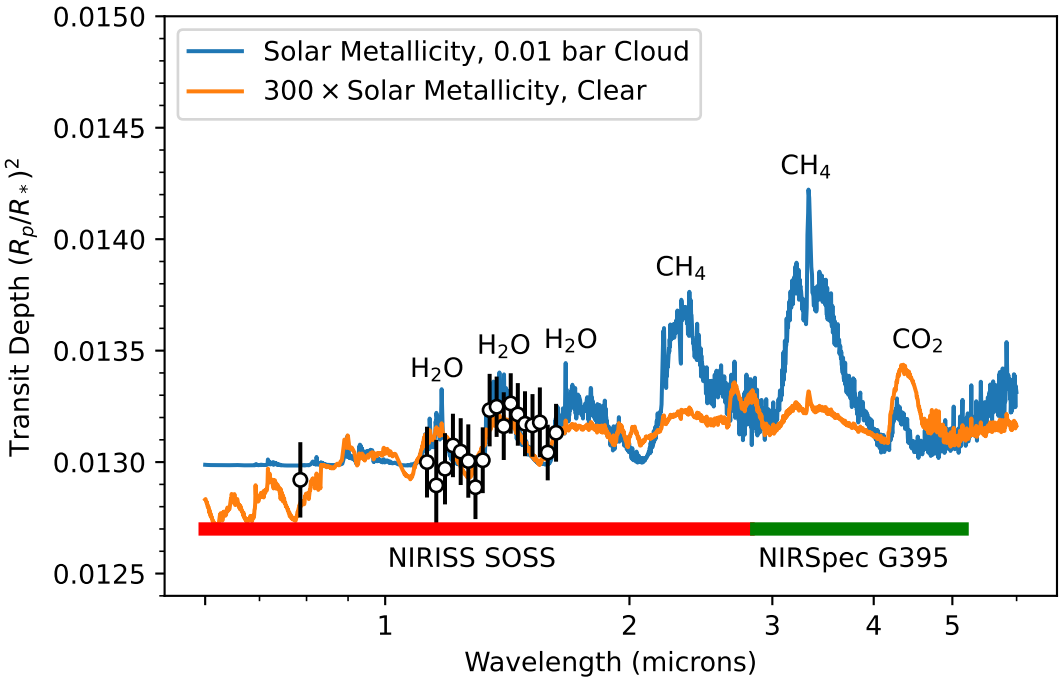

Figure 7. Example *JWST* Cases: one with solar metallicity and high altitude clouds, and one with high metallicity and a clear atmosphere. Both are consistent with our observed *HST* WFC3 data, and need the precision that JWST provides to disambiguate the two models and precisely measure the abundances of the marked absorbers.

REFERENCES

Allart, R., Bourrier, V., Lovis, C., et al. 2018, Science, 362, 1384, doi: 10.1126/science.aat5879

Astropy Collaboration, Robitaille, T. P., Tollerud, E. J., et al. 2013, A&A, 558, A33, doi: 10.1051/0004-6361/201322068

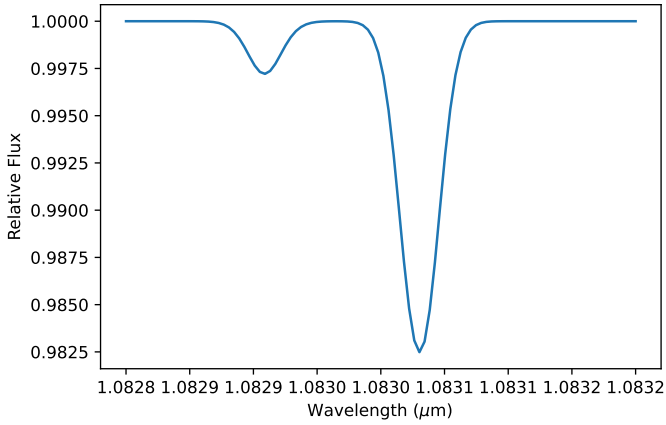

Figure 8. Expected helium signature for a 4000 K thermosphere and a 10^{10} g/s mass loss rate.

Astropy Collaboration, Price-Whelan, A. M., Sipőcz, B. M., et al. 2018, AJ, 156, 123, doi: 10.3847/1538-3881/aabc4f

Bailey, E., & Batygin, K. 2018, ApJL, 866, L2, doi: 10.3847/2041-8213/aade90

Bakos, G. Á., Torres, G., Pál, A., et al. 2010, ApJ, 710, 1724, doi: 10.1088/0004-637X/710/2/1724

Bakos, G. Á., Penev, K., Bayliss, D., et al. 2015, ApJ, 813, 111, doi: 10.1088/0004-637X/813/2/111

Barragán, O., Gandolfi, D., Dai, F., et al. 2018, A&A, 612, A95, doi: 10.1051/0004-6361/201732217

Benneke, B., & Seager, S. 2013, ApJ, 778, 153, doi: 10.1088/0004-637X/778/2/153

Benneke, B., Knutson, H. A., Lothringer, J., et al. 2019, Nature Astronomy, 3, 813, doi: 10.1038/s41550-019-0800-5

Bitsch, B., Raymond, S. N., Buchhave, L. A., et al. 2021, A&A, 649, L5, doi: 10.1051/0004-6361/202140793

Bonomo, A. S., Sozzetti, A., Lovis, C., et al. 2014, A&A, 572, A2, doi: 10.1051/0004-6361/201424617

Borucki, W. J., Koch, D. G., Brown, T. M., et al. 2010, ApJL, 713, L126, doi: 10.1088/2041-8205/713/2/L126

Boss, A. P. 2003, ApJ, 599, 577, doi: 10.1086/379163

Bourque, M., Espinoza, N., Filippazzo, J., et al. 2021, The Exoplanet Characterization Toolkit (ExoCTK), 1.0.0, Zenodo, doi: 10.5281/zenodo.4556063

Buchner, J., Georgakakis, A., Nandra, K., et al. 2014, A&A, 564, A125, doi: 10.1051/0004-6361/201322971

Crossfield, I. J. M., & Kreidberg, L. 2017, AJ, 154, 261, doi: 10.3847/1538-3881/aa9279

Crossfield, I. J. M., Ciardi, D. R., Petigura, E. A., et al. 2016, ApJS, 226, 7, doi: 10.3847/0067-0049/226/1/7

Deming, D., Wilkins, A., McCullough, P., et al. 2013, ApJ, 774, 95, doi: 10.1088/0004-637X/774/2/95

Eigmüller, P., Gandolfi, D., Persson, C. M., et al. 2017, AJ, 153, 130, doi: 10.3847/1538-3881/aa5d0b

Fazio, G. G., Hora, J. L., Allen, L. E., et al. 2004, ApJS, 154, 10, doi: 10.1086/422843

Feroz, F., Hobson, M. P., & Bridges, M. 2009, MNRAS, 398, 1601, doi: 10.1111/j.1365-2966.2009.14548.x

Foreman-Mackey, D., Luger, R., Agol, E., et al. 2021, The Journal of Open Source Software, 6, 3285, doi: 10.21105/joss.03285

Fortney, J. J., Mordasini, C., Nettelmann, N., et al. 2013, ApJ, 775, 80, doi: 10.1088/0004-637X/775/1/80

Fortney, J. J., Visscher, C., Marley, M. S., et al. 2020, AJ, 160, 288, doi: 10.3847/1538-3881/abc5bd

Fraine, J., Deming, D., Benneke, B., et al. 2014, Nature, 513, 526, doi: 10.1038/nature13785

France, K., Loyd, R. O. P., Youngblood, A., et al. 2016, ApJ, 820, 89, doi: 10.3847/0004-637X/820/2/89

Frelikh, R., & Murray-Clay, R. A. 2017, AJ, 154, 98, doi: 10.3847/1538-3881/aa81c7

Fulton, B. J., Petigura, E. A., Howard, A. W., et al. 2017, AJ, 154, 109, doi: 10.3847/1538-3881/aa80eb

Ginzburg, S., Schlichting, H. E., & Sari, R. 2018, MNRAS, 476, 759, doi: 10.1093/mnras/sty290

Greene, T. P., Line, M. R., Montero, C., et al. 2016, ApJ, 817, 17, doi: 10.3847/0004-637X/817/1/17

Hartman, J. D., Bakos, G. Á., Kipping, D. M., et al. 2011, ApJ, 728, 138, doi: 10.1088/0004-637X/728/2/138

Jenkins, J. S., Díaz, M. R., Kurtovic, N. T., et al. 2020, Nature Astronomy, 4, 1148, doi: 10.1038/s41550-020-1142-z

Kempton, E. M. R., Bean, J. L., Louie, D. R., et al. 2018, PASP, 130, 114401, doi: 10.1088/1538-3873/aadf6f

Knutson, H. A., Benneke, B., Deming, D., & Homeier, D. 2014, Nature, 505, 66, doi: 10.1038/nature12887

Kreidberg, L., Line, M. R., Thorngren, D., Morley, C. V., & Stevenson, K. B. 2018, ApJL, 858, L6, doi: 10.3847/2041-8213/aabfce

Kreidberg, L., Bean, J. L., Désert, J.-M., et al. 2014, Nature, 505, 69, doi: 10.1038/nature12888

Lamers, H. J. G. L. M., Vink, J. S., de Koter, A., & Cassinelli, J. P. 1999, Disks formed by Rotation Induced Bi-Stability, ed. B. Wolf, O. Stahl, & A. W. Fullerton, Vol. 523, 159, doi: 10.1007/BFb0106371

Lee, E. J., & Connors, N. J. 2021, ApJ, 908, 32, doi: 10.3847/1538-4357/abd6c7

Mayor, M., & Queloz, D. 1995, Nature, 378, 355, doi: 10.1038/378355a0

Mazeh, T., Holczer, T., & Faigler, S. 2016, A&A, 589, A75, doi: 10.1051/0004-6361/201528065

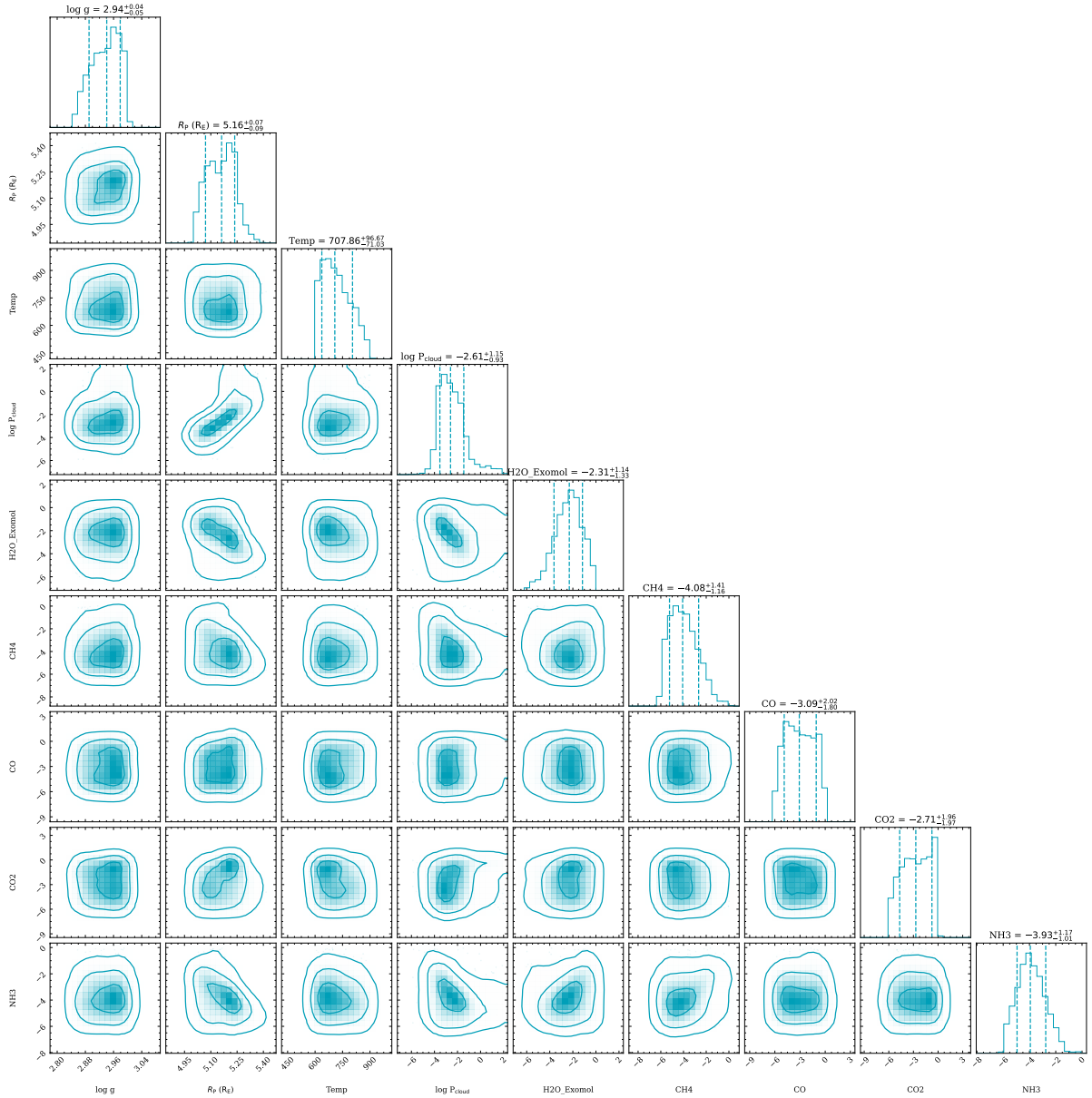

Figure 9. 2-D posteriors for the full retrieval model.

McCullough, P., & MacKenty, J. 2012, Considerations for using Spatial Scans with WFC3, Space Telescope WFC Instrument Science Report

Mollière, P., Wardenier, J. P., van Boekel, R., et al. 2019, A&A, 627, A67, doi: 10.1051/0004-6361/201935470

Mollière, P., Stolker, T., Lacour, S., et al. 2020, A&A, 640, A131, doi: 10.1051/0004-6361/202038325

Morley, C. V., Knutson, H., Line, M., et al. 2017, AJ, 153, 86, doi: 10.3847/1538-3881/153/2/86

Moses, J. I., Line, M. R., Visscher, C., et al. 2013, ApJ, 777, 34, doi: 10.1088/0004-637X/777/1/34

Murgas, F., Astudillo-Defru, N., Bonfils, X., et al. 2021, A&A, 653, A60, doi: 10.1051/0004-6361/202140718

Oklopčić, A., & Hirata, C. M. 2018, ApJL, 855, L11, doi: 10.3847/2041-8213/aaada9

Owen, J. E., & Lai, D. 2018, MNRAS, 479, 5012, doi: 10.1093/mnras/sty1760

Owen, J. E., & Wu, Y. 2017, ApJ, 847, 29, doi: 10.3847/1538-4357/aa890a

Parker, E. N. 1958, ApJ, 128, 664, doi: 10.1086/146579

Ricker, G. R., Winn, J. N., Vanderspek, R., et al. 2015, Journal of Astronomical Telescopes, Instruments, and Systems, 1, 014003, doi: 10.1117/1.JATIS.1.1.014003

Salvatier, J., Wieckiâ, T. V., & Fonnesbeck, C. 2016, PyMC3: Python probabilistic programming framework. http://ascl.net/1610.016

Seager, S. 2010, Exoplanet Atmospheres: Physical Processes

Spake, J. J., Sing, D. K., Evans, T. M., et al. 2018, Nature, 557, 68, doi: 10.1038/s41586-018-0067-5

Stassun, K. G., Oelkers, R. J., Pepper, J., et al. 2018, AJ, 156, 102, doi: 10.3847/1538-3881/aad050

Stevenson, K. B., Bean, J. L., Seifahrt, A., et al. 2016, ApJ, 817, 141, doi: 10.3847/0004-637X/817/2/141

Trotta, R. 2008, Contemporary Physics, 49, 71, doi: 10.1080/00107510802066753

Tsiaras, A., Waldmann, I. P., Rocchetto, M., et al. 2016a, ApJ, 832, 202, doi: 10.3847/0004-637X/832/2/202

Tsiaras, A., Rocchetto, M., Waldmann, I. P., et al. 2016b, ApJ, 820, 99, doi: 10.3847/0004-637X/820/2/99

Tsiaras, A., Waldmann, I. P., Zingales, T., et al. 2018, AJ, 155, 156, doi: 10.3847/1538-3881/aaaf75

Wakeford, H. R., Sing, D. K., Kataria, T., et al. 2017, Science, 356, 628, doi: 10.1126/science.aah4668

West, R. G., Gillen, E., Bayliss, D., et al. 2019, MNRAS, 486, 5094, doi: 10.1093/mnras/stz1084